Supporting Material

Extracting cell stiffness from Real-Time Deformability Cytometry — a theoretical and experimental analysis

A. Mietke[1], O. Otto[1], S. Girardo[1], P. Rosendahl[1], A. Taubenberger[1], E. Ulbricht[1], S. Golfier[1], S. Aland[2], J. Guck[1], and E. Fischer-Friedrich[3,4,*]

[1] *Biotechnology Center, Technische Universität Dresden, Dresden, Germany*

[2] *Institute of Scientific Computing, Technische Universität Dresden, Dresden, Germany*

[3] *Max Planck Institute for the Physics of Complex Systems, Dresden, Germany and*

[4] *Max Planck Institute of Molecular Cell Biology and Genetics, Dresden, Germany*

S1. PERTURBATION APPROACH FOR THE CALCULATION OF THE ELASTIC DEFORMATION OF AN ADVECTED SPHERE

We estimate surface stress and elastic strain of an advected, elastic sphere in terms of a perturbation approach that is valid for small flow rates Q. To make this more precise, we introduce a dimensionless flow rate $\hat{Q} = \frac{\eta Q}{ER^3}$. Here, η is the viscosity of the carrier medium, R is the channel radius and E is the sphere's Young's modulus. Our perturbation calculation takes into account terms up to first order in $\hat{Q}$. The hydrodynamic stress $\boldsymbol{\sigma}^H$ on the sphere's surface is a function of $\hat{Q}$ and of the elastic deformation of the sphere captured by the strain tensor $\boldsymbol{\epsilon}$. Accordingly, we make an expansion

$$\sigma_{ij}^H(\hat{Q}, \boldsymbol{\epsilon}) = A_0(\boldsymbol{\epsilon}) + A_1(\boldsymbol{\epsilon})\hat{Q} + \mathcal{O}(\hat{Q}^2)$$

As hydrodynamic stresses vanish if the flow rate is zero, $A_0(\boldsymbol{\epsilon})$ equals zero. Further, $\boldsymbol{\epsilon}$ is also a function of $\hat{Q}$ with

$$\boldsymbol{\epsilon}(\hat{Q}) = \mathcal{O}(\hat{Q}).$$

Accordingly

$$A_1(\boldsymbol{\epsilon}) = A_{1,0} + \mathcal{O}(\boldsymbol{\epsilon}) = A_{1,0} + \mathcal{O}(\hat{Q}).$$

Therefore,

$$\sigma_{ij}^H(\hat{Q}, \boldsymbol{\epsilon}(\hat{Q})) = A_{1,0}\hat{Q} + \mathcal{O}(\hat{Q}^2).$$

We conclude, that for a perturbation approach up to first order in $\hat{Q}$, we may estimate the stress on the sphere's surface using an undeformed sphere ($\boldsymbol{\epsilon} = 0$).
Although less intuitive, $\hat{Q}$ may also be regarded as a function of $\boldsymbol{\epsilon}$ with

$$\hat{Q}(\boldsymbol{\epsilon}) = \mathcal{O}(\boldsymbol{\epsilon}).$$

Therefore, a first order perturbation calculation in $\hat{Q}$ is equivalent to a first order perturbation calculation in elastic strain $\boldsymbol{\epsilon}$ which is a common approach in elasticity theory.

S2. CALCULATION OF THE STRESS ACTING ON THE SURFACE OF AN ADVECTED SPHERE

In the following, we explain in detail how to determine the expansion coefficients (A_n, B_n, C_n, D_n) of the stream function Ψ introduced in Eq. (18) (main text).

Characteristic scales and dimensional reduction. To simplify the notation and to find the minimal set of independent parameters, we define the characteristic scales composed of the radius of the sphere r_0, the velocity of the sphere v in the rest frame of the channel, and the fluid viscosity η. With this, we find a characteristic force $F_c \equiv r_0 \eta v$ and a characteristic stress $\sigma_c \equiv \frac{\eta v}{r_0}$. The latter can be used to define a dimensionless elastic modulus by $\hat{E} \equiv E/\sigma_c$, a dimensionless shear modulus by $\hat{G} \equiv G/\sigma_c$, as well as a dimensionless pressure by $\hat{p} \equiv p/\sigma_c$. Further, we introduce a dimensionless stream function $\hat{\Psi}$ given by $\hat{\Psi} \equiv \Psi/(v r_0^2)$. Accordingly, we define dimensionless expansion coefficients $(\hat{A}_n, \hat{B}_n, \hat{C}_n, \hat{D}_n)$ that relate to Eq. (18) (main text) by $A_n \equiv v r_0^{2-n} \hat{A}_n$, $B_n \equiv v r_0^{n+1} \hat{B}_n$, $C_n \equiv v r_0^{-n} \hat{C}_n$ and $D_n \equiv v r_0^{n-1} \hat{D}_n$. In addition, we introduce the notation $\hat{\mathbf{A}}_n := (\hat{A}_n, \hat{B}_n, \hat{C}_n, \hat{D}_n)$, so that $\{\hat{\mathbf{A}}_n\}$ denotes the set of all dimensionless expansion coefficients.

Calculating the constants $(\hat{A}_n, \hat{B}_n, \hat{C}_n, \hat{D}_n)$ for a force-free motion of the sphere through the channel. The linear system of equations that is found by the procedure outlined in Appendix A of the main text reads [2]

$$
\begin{aligned}
&\hat{u} + \sum_{\substack{n=0 \\ n \text{ even}}}^{\infty} (\mathcal{A}_n^{(\alpha_0)} a_n + \mathcal{B}_n^{(\alpha_0)} b_n) = -1 && \sum_{\substack{n=0 \\ n \text{ even}}}^{\infty} (\mathcal{A}_n^{(\beta_0)} a_n + \mathcal{B}_n^{(\beta_0)} b_n) = -\frac{2}{5}\lambda^2 \\
&\sum_{\substack{n=0 \\ n \text{ even}}}^{\infty} (\mathcal{A}_n^{(\alpha_1)} a_n + \mathcal{B}_n^{(\alpha_1)} b_n) = \frac{2}{5}\lambda^2 && \sum_{\substack{n=0 \\ n \text{ even}}}^{\infty} (\mathcal{A}_n^{(\beta_1)} a_n + \mathcal{B}_n^{(\beta_1)} b_n) = 0 \\
&\sum_{\substack{n=0 \\ n \text{ even}}}^{\infty} (\mathcal{A}_n^{(\alpha_2)} a_n + \mathcal{B}_n^{(\alpha_2)} b_n) = 0 && \sum_{\substack{n=0 \\ n \text{ even}}}^{\infty} (\mathcal{A}_n^{(\beta_2)} a_n + \mathcal{B}_n^{(\beta_2)} b_n) = 0 \\
&\qquad\qquad\qquad\qquad \vdots \\
&\sum_{\substack{n=0 \\ n \text{ even}}}^{\infty} (\mathcal{A}_n^{(\alpha_k)} a_n + \mathcal{B}_n^{(\alpha_k)} b_n) = 0 && \sum_{\substack{n=0 \\ n \text{ even}}}^{\infty} (\mathcal{A}_n^{(\beta_k)} a_n + \mathcal{B}_n^{(\beta_k)} b_n) = 0 \\
&\qquad\qquad\qquad\qquad \vdots
\end{aligned}
\tag{S1}
$$

with

$$\mathcal{A}_n^{(\alpha_k)} = \delta_{2k,n}\frac{(4k+5)(2k+2)!}{4}\pi + \left(\frac{I_1^{(2k+n+1)}}{(2k-2)!(4k+1)} - \frac{I_2^{(2k+n+2)}}{(2k)!}\right)\lambda^{n+2k+3}$$

$$\mathcal{A}_n^{(\beta_k)} = \delta_{2k,n}\frac{(4k+3)(2k+2)!}{4}\pi - \frac{I_1^{(2k+n)}}{(2k!)(4k+5)}\lambda^{n+2k+5}$$

$$\mathcal{B}_n^{(\alpha_k)} = \left(\delta_{2k,n}\frac{(4k+3)(2k+2)!}{4(4k+1)} + \delta_{2k,n-2}\frac{(2k+2)(2k+1)(2k+2)!}{4}\right)\pi + \left(\frac{I_3^{(2k+n+1)}}{(2k)!} + \frac{(2k+2)(2k+1)}{(2k)!(4k+1)}I_2^{(2k+n)}\right)\lambda^{n+2k+1}$$

$$\mathcal{B}_n^{(\beta_k)} = \left(\delta_{2k,n}\frac{(2k+2)!}{4} + \delta_{2k,n-2}\frac{(2k+2)(4k+3)(2k+1)(2k+2)!}{4(4k+5)}\right)\pi - \frac{I_2^{(2k+n-1)}}{(2k)!(4k+5)}\lambda^{n+2k+3},$$

where $I_1^{(s)}, I_2^{(s)}, I_3^{(s)}$ are integrals that are given explicitly in [2] (p. 17 therein) and that need to be evaluated numerically. $\delta_{i,j}$ is the usual Kronecker symbol. In Eq. (S1), we have introduced the dimensionless quantities $\lambda = r_0/R$ with the radius of the advected sphere r_0 and the channel radius R, as well as $\hat{u} = u/v$ with the velocity of the sphere v and the maximum flow velocity u of the Poiseuille flow at infinity. The above system of equations (S1) is solved in terms of $(a_0, a_2, ..., b_0, b_2, ...)$.

The expansion coefficients $(\hat{A}n, \hat{B}_n, \hat{C}_n, \hat{D}_n)$ can then be obtained from [2]

$$\hat{B}_n = (-1)^{\frac{n}{2}+1}\pi\left(\frac{n!}{2}a_{n-2} + \frac{n(n-1)n!}{2(2n+1)}b_n\right) \tag{S2a}$$

$$\hat{D}_n = (-1)^{\frac{n}{2}+1}\frac{\pi n!}{2(2n-3)}b_{n-2} \tag{S2b}$$

$$\hat{A}_n = -\frac{2n+1}{2}\hat{B}_n + \frac{1-2n}{2}\hat{D}_n \tag{S2c}$$

$$\hat{C}_n = \frac{2n-1}{2}\hat{B}_n + \frac{2n-3}{2}\hat{D}_n. \tag{S2d}$$

An additional constraint on the system of equations (S1) emerges from the condition of a force free steady-state motion of the sphere. As an expansion of the stress of the surface of

the sphere, we introduced in the main text

$$\sigma_{rr}^{H}\big|_{r=r_0} = \sigma_c \sum_{\substack{n=1 \\ n\,\text{odd}}}^{\infty} f_n P_n(\cos\theta)$$
$$\sigma_{r\theta}^{H}\big|_{r=r_0} = \sigma_c \sum_{\substack{n=1 \\ n\,\text{odd}}}^{\infty} g_n \frac{dP_n(\cos\theta)}{d\theta},$$

with

$$f_n(\hat{\mathbf{A}}_{n+1}) = 2\left(\frac{2n+3}{n}\hat{C}_{n+1} + \frac{2n-1}{n+1}\hat{D}_{n+1}\right) \tag{S3a}$$
$$g_n(\hat{\mathbf{A}}_{n+1}) = -\left(\frac{n-1}{n}\hat{A}_{n+1} + \frac{n+2}{n+1}\hat{B}_{n+1} + \frac{n+3}{n}\hat{C}_{n+1} + \frac{n-2}{n+1}\hat{D}_{n+1}\right). \tag{S3b}$$

Integrating the general expansion of surface stress over the surface of the sphere and imposing a vanishing net force leads to the constraint relation $f_1 + 2g_1 \overset{!}{=} 0$. Plugging Eqns. (S3a) and (S3b) into this relation and using $2\hat{C}_2 - 3\hat{B}_2 = 0$ (this can be seen by evaluating $v_r(r_0) = 0$ and $v_\theta(r_0) = 0$) it follows that $\hat{D}_2 \overset{!}{=} 0$. It can be seen from Eq. (S2b) that this is equivalent to $b_0 = 0$. Hence, for a given λ, we simply solve Eqns. (S1) by setting $b_0 = 0$ and treating $\hat{u} = u/v$ as an additional unknown instead, whose value depend on the particular choice of λ.

The described method provides a fast and numerically exact method to simultaneously determine $\hat{u}(\lambda)$ (i.e. the size dependent steady-state velocity) and the expansion coefficients $\{\hat{\mathbf{A}}_n\}$ for the case where no net force acts on the sphere. Truncating the summations in Eqns. (S1) at some even $n = n_{\max}$ and taking into account the first $n_{\max} + 2$ equations up to $k_{\max} = (n_{\max} + 2)/2 - 1$ yields a closed system that determines the $n_{\max} + 2$ unknowns $(\hat{u}, a_0, a_2, ..., a_{n_{\max}}, b_2, b_4, ..., b_{n_{\max}})$, which directly yield $\{\hat{\mathbf{A}}_n\}_{n=2,4,...,n_{\max}}$ via Eqns. (S2a)-(S2d). The physical steady state velocity of the advected sphere for a particular peak flow velocity u in the channel is then determined by $v(\lambda) = u/\hat{u}(\lambda)$. We have checked that the coefficients converge when $n_{\max}$ is increased. As shown in the following, the absolute values of $(\hat{A}_n, \hat{B}_n, \hat{C}_n, \hat{D}_n)$ additionally decrease for larger n, which justifies the suggested truncation scheme.

Evaluation of expansion coefficients and hydrodynamic stresses for different $\boldsymbol{\lambda}$. Fig. S1 shows the amplitudes of the coefficient vector $|\hat{\mathbf{A}}_n| = \sqrt{\hat{A}_n^2 + \hat{B}_n^2 + \hat{C}_n^2 + \hat{D}_n^2}$, normalized by its maximum at $n = 2$. The expansion coefficients decay slower with n for larger λ.

This represents the increasingly complex interaction with the wall for larger spheres. Depending on the application, one can then choose an appropriate threshold to truncate the series. In this work we have chosen to neglect terms with $|\hat{\mathbf{A}}_n|/|\hat{\mathbf{A}}_2| < 10^{-4}$. This threshold leads to a numerical precision of the derived hydrodynamic surface stresses σ_{ij}^H/σ_c of approximately 10^{-3}, which suffices for experimental purposes.

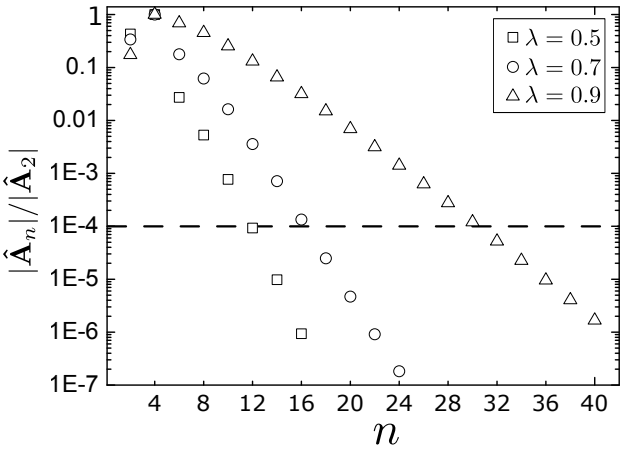

FIG. S1: Normalized absolute value of the coefficient vectors $\hat{\mathbf{A}}_n$ used in the stream function for different λ. For the shown data we neglected all coefficients with $|\hat{\mathbf{A}}_n|/|\hat{\mathbf{A}}_2| < 10^{-4}$. This threshold is depicted by the dashed line, which shows that more and more terms have to be included for the same numerical precision, when λ is increased. $\hat{\mathbf{A}}_n = 0$ for odd n.

Figure S2 depicts the values of the expansion coefficients f_n and g_n as given by Eqns. S3a and S3b for different λ. As mentioned before, $f_n = g_n = 0$ for even n, which is a consequence of the symmetry of the flow solution. Their amplitudes increase for greater values of λ, which represents an increase in stress, if the object's size is increased and all other experimental parameters are left constant.

Fig. S3 shows the stress amplitudes for $\lambda = 0.9$. All other parameters are as for Figure 3A in the main text. Despite the overall increase of stress amplitudes, the vicinity of the channel walls now leads to much more pronounced effects on surface regions around $\theta = \pi/2$ compared to $\lambda = 0.7$. Again those results are verified by the Finite-Element method.

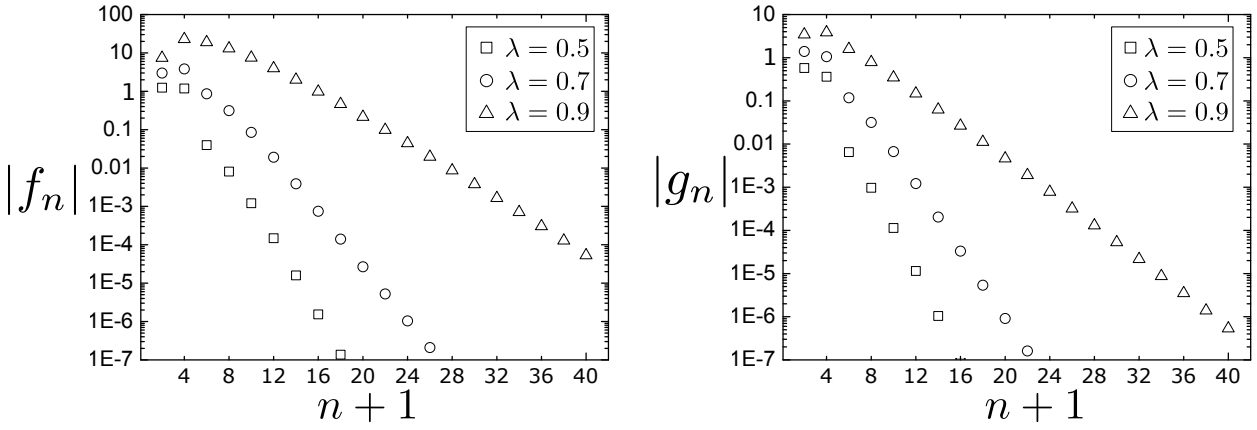

FIG. S2: Expansion coefficients of the hydrodynamic stresses on the surface of the sphere for different λ. f_n relates to pressure, g_n relates to shear stresses. Decay properties are very similar to those of the stream function coefficients Fig. S1. Increasing λ leads to an overall increase of coefficient amplitudes and hence stress, when experimental conditions (Flow rate Q and viscosity η) are kept constant. $f_n = g_n = 0$ for for even n.

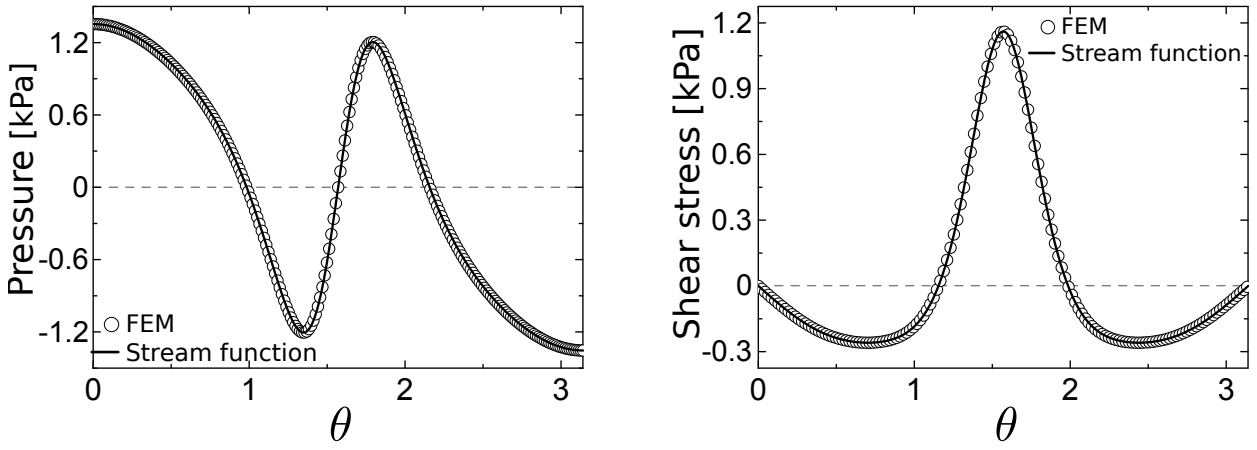

FIG. S3: Hydrodynamic pressure (left) and shear stress (right) for $\lambda = 0.9$. Solid line shows results from the stream function approach for $Q = 0.012\,\mu\text{l/s}$ and $\eta = 0.015\,\text{mPa}\cdot\text{s}$ (typical experimental parameters, as used in Fig. 3B (main text)) and channel radius $R = 10\,\mu\text{m}$. While the essential characteristics are still given by the 1st and 3rd Legendre polynomials and their derivatives, normal and tangential stress amplitudes increase by a factor of 2 and 4, respectively, compared to $\lambda = 0.7$. The strong stress gradients around $\pi/2$ (near the channel walls) lead to the bulge and groove for deformed shapes shown in Fig. 4A (main text).

S3. EQUIVALENT CHANNEL RADIUS

To map the situation of a steady flow in a channel with square cross-section of side length L onto the problem of a steady flow in a cylindrical channel with radius R_{eq}, we take the following approach: we derive a factor C with $2R_{eq} = C \cdot L$ such that the pressure drop is the same in the circular channel as in the square channel. Textbook results for the fluid flow through channels with circular and square cross-section [3] can be used to derive

$$C = 2\sqrt[4]{\frac{2K_1}{3\pi}} \approx 1.094$$

with

$$K_1 = 1 - 6\sum_{n=1}^{\infty} \frac{\tanh(\omega_n)}{\omega_n^5} \text{ with } \omega_n = (2n-1)\frac{\pi}{2}.$$

This defines $\lambda_{eq} = r_0/R_{eq}$ and we can identify the different geometries by $\lambda = \lambda_{eq}$.

S4. LEGENDRE POLYNOMIALS

We solve the stream function, stress components and displacements fields of the advected elastic spherical object in terms of an expansion of Legendre polynomials. The defining differential equation of Legendre polynomials $P_n(x)$, $x \in [-1, 1]$ reads

$$\frac{\mathrm{d}}{\mathrm{d}x}\left[(1-x^2)\frac{\mathrm{d}P_n(x)}{\mathrm{d}x}\right] + n(n+1)P_n(x) = 0. \tag{S4}$$

To derive most of the equations related to displacement calculations in all models, we have to make use of an identity that follows directly from (S4) by substituting $x \to \cos\theta$ and reads

$$\frac{\mathrm{d}^2 P_n(\cos\theta)}{\mathrm{d}\theta^2} = -\left(\cot\theta \frac{\mathrm{d}P_n(\cos\theta)}{\mathrm{d}\theta} + n(n+1)P_n(\cos\theta)\right).$$

S5. EQUILIBRIUM EQUATIONS OF LINEAR ELASTICITY IN SPHERICAL COORDINATES

For the sake of completeness, we state the equilibrium equation of linear elasticity in spherical coordinates, i.e. the components of

$$\nabla \cdot \boldsymbol{\sigma} = 0 \tag{S5}$$

where ∇ represents the covariant derivative the stress tensor $\boldsymbol{\sigma}$. The components of Eq. (S5) in spherical coordinates read [4]

$$\begin{aligned}\frac{\partial\sigma_{rr}}{\partial r}+\frac{1}{r}\frac{\partial\sigma_{r\theta}}{\partial\theta}+\frac{1}{r\sin\theta}\frac{\partial\sigma_{r\varphi}}{\partial\varphi}+\frac{2\sigma_{rr}-\sigma_{\theta\theta}-\sigma_{\varphi\varphi}+\sigma_{r\theta}\cot\theta}{r}&=0\\ \frac{\partial\sigma_{r\theta}}{\partial r}+\frac{1}{r}\frac{\partial\sigma_{\theta\theta}}{\partial\theta}+\frac{1}{r\sin\theta}\frac{\partial\sigma_{\theta\varphi}}{\partial\varphi}+\frac{3\sigma_{r\theta}+(\sigma_{\theta\theta}-\sigma_{\varphi\varphi})\cot\theta}{r}&=0\\ \frac{\partial\sigma_{r\varphi}}{\partial r}+\frac{1}{r}\frac{\partial\sigma_{\theta\varphi}}{\partial\theta}+\frac{1}{r\sin\theta}\frac{\partial\sigma_{\varphi\varphi}}{\partial\varphi}+\frac{3\sigma_{r\varphi}+2\sigma_{\theta\varphi}\cot\theta}{r}&=0.\end{aligned}$$

Stress-strain relations for an isotropic, linearly elastic material read in all coordinates [6]

$$\sigma_{ij}=2G\left(\epsilon_{ij}+\frac{\nu}{1-2\nu}\delta_{ij}\epsilon_{kk}\right). \tag{S6}$$

The components of the strain tensor relevant for the calculations of surface stresses relate to the displacement fields by

$$\epsilon_{rr}=\frac{\partial u_r}{\partial r}\qquad \epsilon_{\theta\theta}=\frac{1}{r}\frac{\partial u_\theta}{\partial\theta}+\frac{u_r}{r}\qquad \epsilon_{r\theta}=\epsilon_{\theta r}=\frac{1}{2}\left(\frac{\partial u_\theta}{\partial r}-\frac{u_\theta}{r}+\frac{1}{r}\frac{\partial u_r}{\partial\theta}\right). \tag{S7}$$

S6. THE PAPKOVICH-NEUBER ANSATZ

Solutions to the force balance equation (S5) can in general be given by a Papkovich-Neuber ansatz [7]

$$\mathbf{u}=4(1-\nu)\mathbf{B}-\nabla(\mathbf{r}\cdot\mathbf{B}+B_0), \tag{S8}$$

where $\mathbf{B}$ and B_0 are a harmonic vector and a harmonic scalar potential, i.e. $\nabla^2\mathbf{B}$ and $\nabla^2 B_0$ vanish. A harmonic scalar B_0 in spherical coordinates with azimuthal symmetry can be written as [4]

$$B_0=\sum_{n=0}^{\infty}\left[\bar{a}_n r^n+\frac{\bar{b}_n}{r^{n+1}}\right]P_n(\cos\theta).$$

Harmonic vectors in spherical coordinates with azimuthal symmetric components can be derived by making the ansatz

$$B_r=\sum_{\substack{n=0\\k=-\infty}}^{\infty}a_{nk}r^k P_n(\cos\theta)\qquad\text{and}\qquad B_\theta=\sum_{\substack{n=1\\l=-\infty}}^{\infty}b_{nl}r^l\frac{dP_n(\cos\theta)}{d\theta}$$

in the vector Laplace equation $\nabla^2\mathbf{B}=0$. Taking into account the orthogonality of the Legendre polynomials, we find a biquadratic equation in $l=k$, which yields expansions of

the components of $\mathbf{B}$ of the form

$$B_r = \sum_{n=0}^{\infty} \left[n\bar{c}_n r^{n-1} - (n+1)\frac{\bar{d}_n}{r^{n+2}} \right] P_n(\cos\theta) \tag{S9}$$

$$B_\theta = \sum_{n=1}^{\infty} \left[\bar{c}_n r^{n-1} + \frac{\bar{d}_n}{r^{n+2}} \right] \frac{dP_n(\cos\theta)}{d\theta} \tag{S10}$$

and

$$B_r = \sum_{n=0}^{\infty} \left[-\bar{e}_n (n+1) r^{n+1} + n\frac{\bar{f}_n}{r^n} \right] P_n(\cos\theta)$$

$$B_\theta = \sum_{n=1}^{\infty} \left[\bar{e}_n r^{n+1} + \frac{\bar{f}_n}{r^n} \right] \frac{dP_n(\cos\theta)}{d\theta}.$$

Note that Eqns. (S9) and (S10) are directly proportional to the respective components of ∇B_0 and therefore they do not yield a new independent solution in the Papkovich-Neuber ansatz. The coefficients of the displacement fields used in Eqns. (8a) and (8b) (main text), a_n and b_n, relate to the potentials discussed here by $a_n = \bar{e}_n$ and $b_n = \bar{a}_n$, as those are the only independent terms that converge for $r \to 0$. The terms associated with $\bar{b}_n$ and $\bar{f}_n$ can be used in the Papkovich-Neuber ansatz to calculate elastic deformations of thick shells, as for example in [5].

S7. POLAR REPRESENTATION

Figure S4 sketches the geometry we have to consider to derive a polar representation of the deformed shape. We have

$$\varrho(\theta) = \sqrt{[r_0 + u_r(\theta')]^2 + u_\theta(\theta')^2} = r_0 + u_r(\theta') + \mathcal{O}(u^2/r_0). \tag{S11}$$

Additionally we have to include the shift in the angle $\theta = \theta' + \Delta\theta'$, that results from tangential displacements:

$$\tan(\Delta\theta') = \frac{u_\theta(\theta')}{r_0 + u_r(\theta')} \Rightarrow \theta' = \theta - \frac{u_\theta(\theta')}{r_0} + \mathcal{O}(u^2/r_0). \tag{S12}$$

Plugging Eq. (S12) into Eq. (S11) we find $\varrho(\theta)$ and it takes the form $\varrho(\theta) = r_0 + u_r(\theta) + \mathcal{O}(u^2/r_0)$, i.e. other than the radial displacements u_r, tangential displacements u_θ only contribute to second order to a polar representation of the shape.

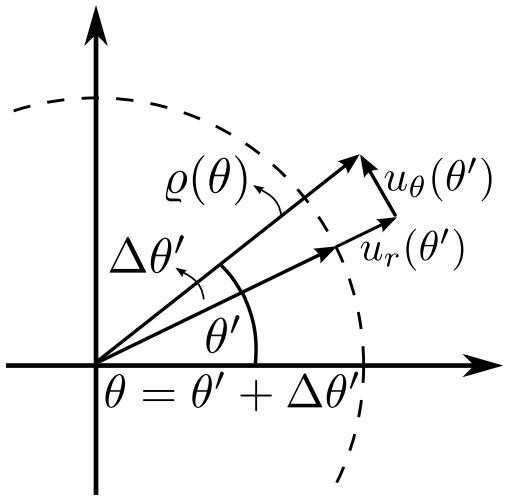

FIG. S4: Conversion between polar shape representation $\varrho(\theta)$ and deformation in terms of displacement fields $u_r(\theta')$ and $u_\theta(\theta')$. $\varrho(\theta)$ relates to the displacement fields u_r and u_θ given at $\theta' = \theta - \Delta\theta'$ in a non-trivial way.

S8. ERROR ESTIMATE OF HYDRODYNAMIC SURFACE STRESS AND ESTIMATED YOUNG'S MODULUS

Here, we estimate the error in the surface stress of an advected sphere that stems from neglecting the feedback of elastic deformation on the surrounding fluid flow. For this purpose, we placed shapes of a deformed solid elastic sphere and a deformed shell depicted in Figure 4A (main text) ($\lambda = 0.7$, $d = 0.006$) as rigid bodies into a cylindrical channel implementing a finite-element simulation using COMSOL Multiphysics [11]. The velocity of the deformed shape was chosen such that the net force vanishes within numerical precision. The resulting stress profile σ^d on the surface of the deformed shapes $\mathbf{r}_d(\theta) = r_0\mathbf{e}_r(\theta) + \mathbf{u}(\theta)$ was compared to the stress σ^u on the undeformed sphere $\mathbf{r}_0(\theta) = r_0\mathbf{e}_r(\theta)$ at equal values of θ for normal stresses σ_n^d and shear stresses σ_s^d, respectively. Note, that this mapping between $\mathbf{r}_0$ and $\mathbf{r}_d$ is unique. The resulting profiles are shown in Figure S5A and B. We estimate the relative stress errors as $\delta_i = |\sigma_i^d - \sigma_i^u|/(\sigma_{i,\max}^u - \sigma_{i,\min}^u)$ $(i = n, s)$, where $\sigma_{i,\max}^u$ and $\sigma_{i,\min}^u$ denote the maximal and minimal value of stress on the surface of the undeformed, advected sphere (see Fig. S5C). For the deformed solid elastic sphere, we find that the stress deviates nowhere on the surface more than 9 % and on average only about 3.5 %. For the deformed shell the deviations are slightly larger, with δ_s reaching up to 16 %. However, the surface

regions where those values occur (close to the channel walls) represent a rather small fraction of the whole surface, such that the average deviations are less than 7 %.

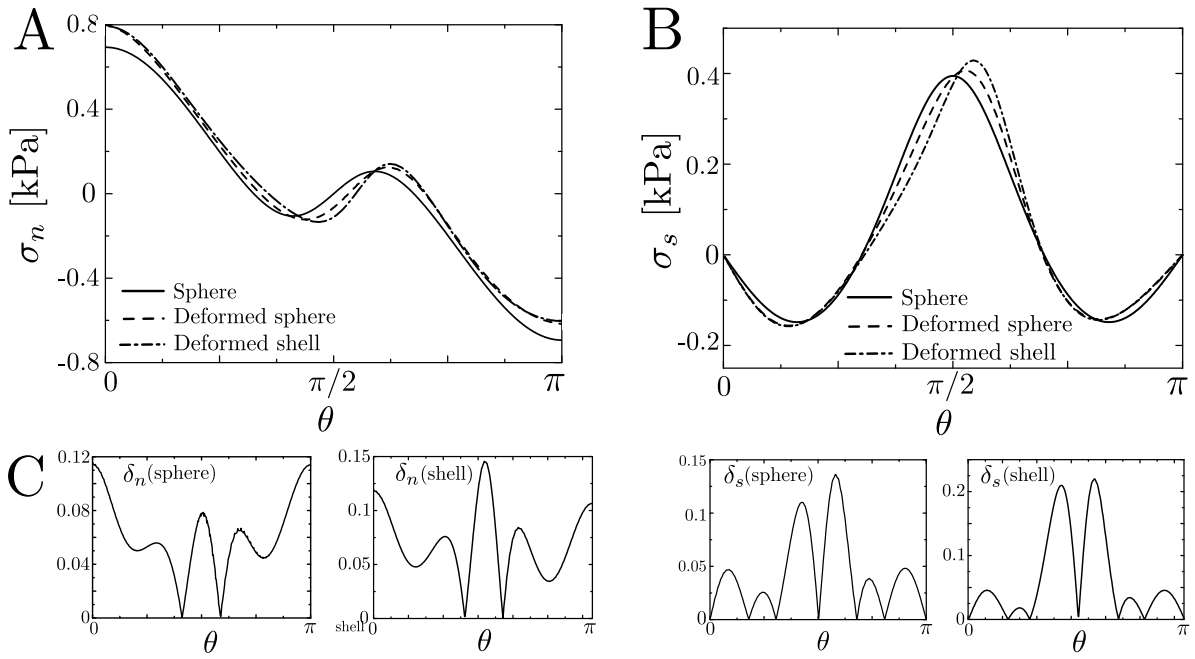

FIG. S5: Comparison of surface stresses σ^u and σ^d on undeformed (solid lines) and deformed shapes (dashed and dot-dashed lines). Objects were advected at steady state in a Poiseuille flow at low Reynold's number. The deformed shapes were generated as a first order deformation of a solid elastic sphere and a thin elastic shell with $\lambda = 0.7$ (see Fig. 4, main text) and dimensional parameters were as Figure 3 (main text): sphere radius $r_0 = 7\,\mu$m, channel radius $R = 20\,\mu$m, flow rate $Q = 0.012\,\mu$l/s, viscosity $\eta = 0.015\,$Pa. (A) Normal hydrodynamic stress. (B) Hydrodynamic shear stress. (C) Deviations $\delta_i = |\sigma_i^d - \sigma_i^u|/(\sigma_{i,\max}^u - \sigma_{i,\min}^u)$ for normal stress $i = n$ (left) and shear stresses $i = s$ (right).

We performed the same analysis for shapes with deformations $d = \{0.01, 0.02, 0.025\}$ and find that the relative error increases with increased deformation (Table S1). Maximal deviations are generally larger on a deformed shell, as compared to a deformed solid elastic sphere of equal deformation and they are localized to surface regions that are close to the channel walls. Due to this localisation the average error across the surface on an elastic shell shape stays small ($< 12\,\%$) within the regime of deformations considered in this work.

To confirm that small errors in surface stresses correspond to small errors in estimated elastic moduli when fitting our analytic theory to experimental shapes, we employed a

	$d = 0.006$	$d = 0.01$	$d = 0.02$	$d = 0.025$
$\delta_n^{\max}, \delta_s^{\max}$ (sphere)	7 %, 9 %	9 %, 12 %	12 %, 18 %	14 %, 21 %
$\delta_n^{\max}, \delta_s^{\max}$ (shell)	8 %, 16 %	12 %, 21 %	19 %, 30.5 %	20 %, 33 %
$\bar{\delta}_n, \bar{\delta}_s$ (sphere)	3 %, 3.5 %	3 %, 4.5 %	4 %, 6.5 %	4.5 %, 7.5 %
$\bar{\delta}_n, \bar{\delta}_s$ (shell)	4 %, 6.5 %	4 %, 8 %	5 %, 11.5 %	7 %, 11.5 %

TABLE S1: Relative errors of hydrodynamic stresses on surfaces of deformed shapes as calculated with the model of a solid elastic sphere (sphere) and a thin elastic shell (shell) for different values of deformation d. $\delta_i^{\max}$ depicts maximal deviation that occur on surface regions close to the cylinder walls $\bar{\delta}_i$ depict deviations averaged over the surface.

fully coupled finite element simulations of a linearly elastic sphere advected in a cylindrical channel (see Sec. S12). This simulation takes into account the coupling between deformation and changes in the surrounding flow field. We used it to generate steady-state shapes for typical experimental parameters, which then were fitted using our analytical theory of an elastic sphere (Fig. S6). For increasing deformations one can identify shape features in the finite-element model that can not completely be captured by the analytical theory, as the changes in the hydrodynamic stresses due to the deformation becomes more relevant (see Table S1). However, when fitting our analytical theory to those shapes the elastic moduli put in the phase field model are quantitatively still very well reproduced with relative errors of less then 4 %.

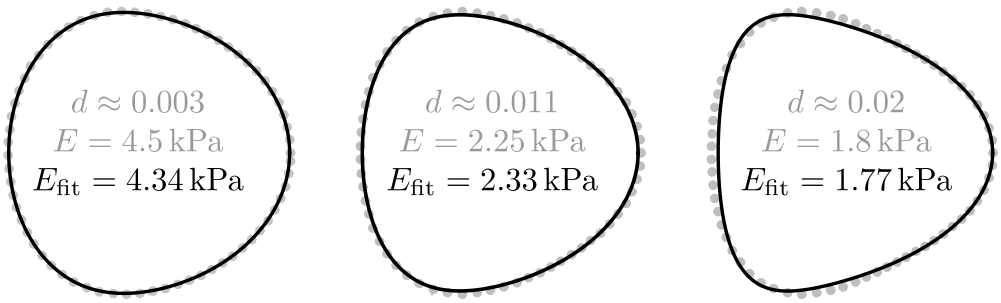

FIG. S6: Fitting of shapes from a fully coupled finite element simulation (see Sec. S12). Steady-state shapes with different deformations were generated using a numerical phase field model (see Sec. S12) (gray dots). The contours were fitted using our analytical theory (solid lines) resulting in a predicted elastic modulus E_{fit}. For all three shapes we have $\lambda \approx 0.7$, $Q = 0.012\,\mu\mathrm{l/s}$, $\eta = 15\,\mathrm{mPa \cdot s}$ and a channel radius $R = 10\,\mu\mathrm{m}$.

S9. AFM INDENTATION EXPERIMENTS.

Agar films were prepared using the same agar solution as for the beads. 600 μl of agar solution were cast into a petri dish (34 mm Ø, TPP Switzerland). Agarose films were then covered with PBS (1 ml) for at least 2 hours before starting the measurement. For the AFM indentation experiments a nanowizard I (JPK Instruments, Berlin) equipped with Cellhesion Module was used. Arrow-T1 cantilevers (Nanoworld, Neuchatel) that had been modified with a polystyrene bead of 10 μm diameter (microparticles GmbH, Berlin) were calibrated prior measurements using the thermal noise method. To determine the stiffness of the agarose films, the cantilever was lowered with a speed of 5 μm/s onto the agarose surface until a relative setpoint of 2.5 nN was reached. The resulting force distance curves were analysed using the JPK image processing software (JPK instruments). Force distance data were corrected for the tip sample separation [10] and fitted with a Hertz model fit for a spherical indenter [8]. A Poisson ratio of 0.5 was assumed (See Sec. S10). Experiments were carried out in PBS and at room temperature. Similar methodical settings were used for indentation experiments on HL60 cells. Arrow -T1 cantilevers were modified with a polystyrene bead of 5 μm diameter and lowered with a speed of 5 μm/s onto the cell surface until a relative setpoint of 2 nN was reached. Force distance data were analyzed as mentioned above. Experiments were carried out at 37°C in CO_2 independent medium (life technologies, Darmstadt) within 1.5 hours.

S10. INFLUENCE OF POISSON RATIO ON FITTED ELASTIC MODULI

In AFM indentation measurements, the Hertz model is used to fit the elastic modulus $E^* = E/(1-\nu^2)$, where E is the Young's modulus and ν is the Poisson ratio [8]. Therefore, assuming a different Poisson ratio ν' leads to a different estimate of the Young's Modulus $E' = E(1-\nu'^2)/(1-\nu^2)$.

For the fitting of data acquired using RT-DC, we assumed incompressibility of beads and cells ($\nu = 0.5$). This is motivated by their large water content together with the very short measurement times of RT-DC (≈ 1 ms) which render it unlikely that water fluxes into and out of the cell play a major role. In order to examine the influence of different choices of ν on our estimate of Young's moduli E, we have performed the same data analysis using $\nu = 0.3$

and $\nu = 0.4$. The results are shown in Table S2. We conclude that changing values of the

	$\nu = 0.3$	$\nu = 0.4$	$\boldsymbol{\nu}$**=0.5**	
Agarose film (AFM, bulk)	2.5 ± 0.1	2.31 ± 0.09	**2.06±0.08**	kPa
Agarose beads (RT-DC, bulk)	1.71±0.92	1.89±1.02	**2.15±1.10**	kPa
HL60 cells (AFM, bulk)	206 ± 103	190 ± 95	**170±85**	Pa
HL60 cells (RT-DC, bulk)	1.11±0.44	1.24±0.50	**1.48±0.51**	kPa
HL60 cells (RT-DC, shell)	21.47±7.88	22.64±8.16	**23.69±8.42**	nN/μm

TABLE S2: Estimated Young's moduli for beads and cells under the assumption of different Poisson ratios ν (mean $\pm$ standard deviation). (legend: AFM, bulk - measured with AFM indentation using the Hertz model, RT-DC, bulk - RT-DC measurement fitted using the model of an isotropic elastic sphere, RT-DC, shell - RT-DC measurement fitted using the model of an isotropic elastic thin shell)

Poisson ratio ν within the interval $[0.3, 0.5]$ does not change the Young's modulus estimate by orders of magnitude but only up to 25%. Therefore, it cannot explain the difference in Young's moduli obtained from AFM and RT-DC measurements on cells. However, a change of Poisson ratios gives rise to opposing trends for AFM and RT-DC measurements. While assuming lower values for the Poisson ratio increases the extracted Young's modulus in AFM measurements, it decreases Young's moduli extracted from RT-DC measurements.

S11. DISTRIBUTION OF STIFFNESS VALUE IN AFM INDENTATION AND RT-DC MEASUREMENTS

We measured cells of a human promyelocytic cell line (HL60) in an RT-DC setup and analyzed deformed cell shapes just as in the case of deformed agar beads described above (see Fig. 5, main text). Employing the cell mechanical model of an isotropic elastic sphere, we obtain on average a cell elastic modulus of $E = 1.47 \pm 0.51\,\mathrm{kPa}$ (N=281, mean±SD). Performing AFM indentation experiments on the cells, we find on average a Young's modulus of $E = 170 \pm 85\,\mathrm{Pa}$ (N=169). Associated distributions of measured cell elastic moduli are shown in Fig. S7. While the means of AFM and RT-DC measurements are different, the distributions of measurement points show similar characteristics. In particular, distri-

butions exhibit a long tail towards higher elastic moduli. This similarity of distributions may indicate that elastic moduli are simply scaled by a constant factor when changing from one measurement technique to the other, something that might be accounted for by the time-scale dependence of cell mechanics [12].

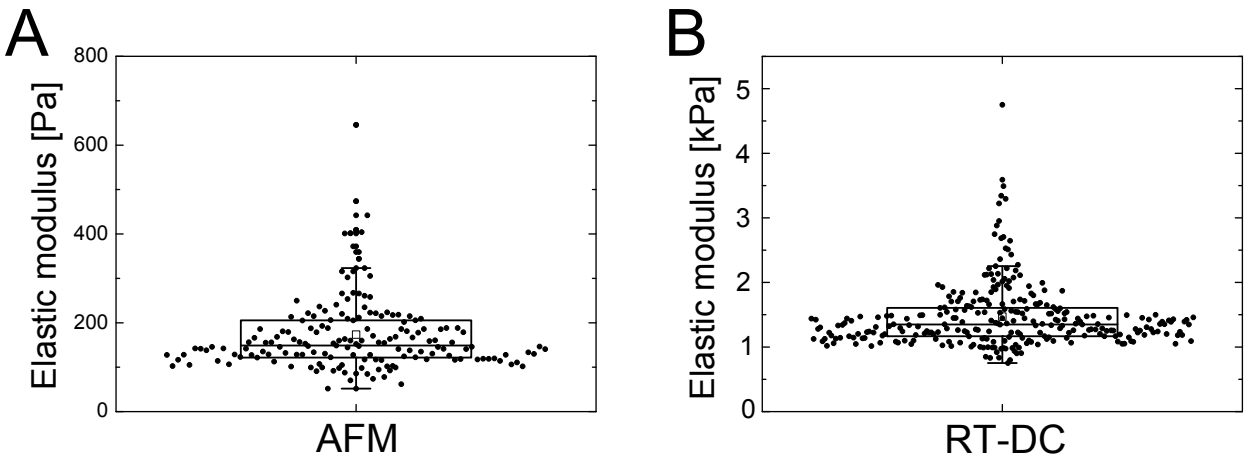

FIG. S7: Distribution of elastic moduli measured with AFM and RT-DC. (A) AFM indentation experiments ($N = 169$, $E = 170 \pm 85\,\mathrm{Pa}$). (B) RT-DC experiment ($N = 281$, $E = 1.47 \pm 0.51\,\mathrm{kPa}$).

S12. FULLY COUPLED FINITE ELEMENT SIMULATIONS

To verify the predicted shapes of our analytic theory, we finally conduct finite element simulations that take into account the coupling between flow field and elastic deformation. Our simulations rely on the Stokes equation for the fluid phase (carrier medium) and linear elasticity theory for an incompressible elastic solid.

The computational method employed is based on a phase field approach, first described in [13]. The elastic sphere and the surrounding fluid are discretized on a common grid and a phase field ϕ is used to distinguish between the phases, i.e. $\phi = 1$ in the fluid, $\phi = 0$ in the cell. Thereby the stationary Stokes equation (1)-(2) can be extended over the full domain, including the elastic stress tensor $\boldsymbol{\sigma}$ in the region where $\phi = 0$.

$$\nabla p - \eta \nabla^2 \mathbf{v} = \nabla \cdot ((1-\phi)\boldsymbol{\sigma})$$

$$\nabla \cdot \mathbf{v} = 0$$

In the fluid phase ($\phi = 1$) we recover the original Stokes equation (1)-(2). In the cell region ($\phi = 0$) in the stationary limit ($\mathbf{v} = 0$) we recover the equation of linear elasicity of an

incompressible material. The use of a common grid here offers several advantages: no re-gridding is needed and the implicit inclusion of the stress balance between viscous fluid and elastic solid, stabilizes the coupling. Further, the elastic stress evolves according to

$$\partial_t \boldsymbol{\sigma} + (\mathbf{v} - \mathbf{v}_c) \cdot \nabla \boldsymbol{\sigma} - \nabla \mathbf{v} \cdot \boldsymbol{\sigma} - \boldsymbol{\sigma} \cdot \nabla \mathbf{v}^T = \frac{E_0}{6} \left(\nabla \mathbf{v} + \nabla \mathbf{v}^T \right) - k\phi \boldsymbol{\sigma}.$$

where $E_0 = 1\,\mathrm{kPa}$ is a reference Young's modulus and we added a penalty constant $k = 10^6\, s^{-1}$ to enforce vanishing stress in the fluid region. Note, that we have subtracted the cell velocity $\mathbf{v}_c$ (computed from the last respective time step) in the advection terms to keep the cell in the middle of our computational domain.

Finally, the phase field is moved with the flow by an advected Cahn-Hilliard equation.

$$\partial_t \phi + (\mathbf{v} - \mathbf{v}_c) \cdot \nabla \phi = M \nabla^2 \mu,$$
$$\mu = \epsilon^{-1}(4\phi^3 - 6\phi^2 + 2\phi) - \epsilon \nabla^2 \phi$$

The included 4th order diffusion with mobility constant $M = 10\mathrm{mm}^3/s$ ensures that the phase field keeps the distinct values of 0 and 1 in the two phases with a smooth but rapid transition at the interface. The thickness of the transition region is controlled by the parameter $\epsilon = 0.05\,\mu\mathrm{m}$ [14].

As initial condition we use a spherical bubble (for ϕ), poisseuille flow (for $\mathbf{v}$) and zero elastic stress ($\boldsymbol{\sigma} = 0$). We prescribe a pressure difference between in- and outflow as boundary condition. This pressure difference is iteratively adapted such as to obtain a prescribed value for E (see Fig. S6) according to the rescaling introduced on page 13, main text.

Consistently with the analytical calculations we consider an axisymmetric setting here which reduces the problem to a two-dimensional computational domain $\Omega = [0, 40]\mu\mathrm{m} \times [0, 10]\mu\mathrm{m}$. Axisymmetric versions of the above evolution equations can be found in [15, 16].

We solve the time-dependent problem with a time step of 1μs until the bubble shape has reached an (almost) stationary state. The compuational grid is adaptively controlled such that the grid size is $0.1\,\mu\mathrm{m}$ close to the cell boundary and $0.8\,\mu\mathrm{m}$ further away from it. More details on the numerical discretization with the Finite-Element toolbox AMDiS can be found in [14].

[1] Happel, J. & H. Brenner *Low Reynolds Number Hydrodynamics* (Nordhoff International Publishing, 1973)

[2] Haberman, L. & R. Sayre Motion of rigid and fluid spheres in stationary and moving liquids inside cylindrical tubes. *D. Taylor (Ed.), Model Basin Rep.* (1958).

[3] Bruus, H. *Theoretical microfluidics* (OUP Oxford, 2008), 1 edition

[4] Arfken, G.B. & Weber, H.J. *Mathematical Methods for Physicists* (Elsevier Ltd., 2005), 3 edition

[5] Ananthakrishnan, R. *et al.* Quantifying the contribution of actin networks to the elastic strength of fibroblasts. *J. Theor. Biol.* **242**, 502 – 516 (2006).

[6] Landau, L. & E. Lifshitz *Theory of Elasticity* (Elsevier Ltd., 1986), 3 edition

[7] Lurie, A. I. *Theory of Elasticity* (Springer, 2005), 1 edition

[8] Sneddon, I. N. The relation between load and penetration in the axisymmetric boussinesq problem for a punch of arbitrary profile. *International Journal of Engineering Science* **3**, 47–57 (1965).

[9] Otto, O. *et al.* Real-time deformability cytometry: High-throughput cell mechanical phenotyping on-the-fly. *Nat Met* **12**, 199-202 (2015).

[10] Domke, J. & M. Radmacher Measuring the elastic properties of thin polymer films with the atomic force microscope. *Langmuir* **14**, 3320–3325 (1998).

[11] www.comsol.com

[12] Kollmannsberger, P., and B. Fabry. Linear and nonlinear rheology of living cells. *Ann Rev Mater Res* **41**, 75–97 (2011).

[13] Sun, P., J. Xu and L. Zhang. Full Eulerian finite element method of a phase field model for fluid-structure interaction problem. *Computers & Fluids* **90**, 1–8 (2014).

[14] Aland, S., and A. Voigt. Benchmark computations of diffuse interface models for two-dimensional bubble dynamics. *Int J Numer Meth Fl* **69**, 747–761 (2012).

[15] Aland, S. *et al.* Modeling and numerical approximations for bubbles in liquid metal. *Eur Phys J Spec Top* **220**, 185–194 (2013).

[16] Tomé, M. *et al.* Die-swell, splashing drop and a numerical technique for solving the Oldroyd B model for axisymmetric free surface flows. *J Non-Newton Fluid* **141**, 148–166 (2007).